2-5-2024

Maximizing charge dynamics in ZnIn2S4/CN Van der Waals heterojunction for optimal hydrogen production from photoreforming of glucose

Jinqiang Zhang

Xinyuan Xu
Edith Cowan University

Lei Shi

Huayang Zhang

Shaobin Wang

See next page for additional authors

10.1016/j.ces.2023.119532
Zhang, J., Xu, X., Shi, L., Zhang, H., Wang, S., & Sun, H. (2024). Maximizing charge dynamics in ZnIn2S4/CN Van der Waals heterojunction for optimal hydrogen production from photoreforming of glucose. Chemical Engineering Science, 284, article 119532. https://doi.org/10.1016/j.ces.2023.119532

Chemical Engineering Science 284 (2024) 119532

Contents lists available at ScienceDirect

Chemical Engineering Science

journal homepage: www.elsevier.com/locate/ces

Maximizing charge dynamics in $ZnIn_2S_4$/CN Van der Waals heterojunction for optimal hydrogen production from photoreforming of glucose

Jinqiang Zhang [a,*], Xinyuan Xu [b,c], Lei Shi [d], Huayang Zhang [a], Shaobin Wang [a,*], Hongqi Sun [b,*]

[a] School of Chemical Engineering, The University of Adelaide, South Australia 5005, Australia
[b] School of Molecular Sciences, The University of Western Australia, 35 Stirling Highway, Perth, Western Australia 6009, Australia
[c] School of Science, Edith Cowan University, Joondalup, Western Australia 6027, Australia
[d] Lab of Biomass Energy and Functional Carbon Materials, College of Materials Science and Engineering, Nanjing Forestry University, Nanjing 210037, China

ARTICLE INFO

Keywords:
Photoreforming
Hydrogen
Heterojunction
Carbon nitride
Biomass

ABSTRACT

Biomass photoreforming stands out as a promising avenue for green hydrogen, leveraging solar energy for the generation and transformation of clean and renewable energy resources. The pursuit of efficient photocatalysts is motivated by the unsatisfied hydrogen evolution performance arising from the complex and stubborn structure of biomass. Herein, we loaded 2-dimensional (2D) $ZnIn_2S_4$ onto 2D carbon nitride nanosheets, resulting in the formation of Van der Waals (VDW) heterojunctions (ZIS/CN). Band structure and morphology of CN were rationally tailored through precursor engineering to effectively magnify interfacial internal electric field and minimize diffusion pathway within the VDW heterostructure, realizing optimal charge dynamics in ZIS/DCN. As a result, intensified H_2 generation was achieved, which was 350 times higher than pure DCN and outperformed ZIS at the same unit mass. This work offers design principles for VDW heterostructured photocatalysts and accelerates the transition towards a more sustainable manner in biomass reforming.

1. Introduction

The excessive consumption of fossil fuels has become a critical challenge in today's world, necessitating a shift towards prioritizing green energy sources. (Cai et al., 2021; Zhou et al., 2023; Sun et al., 2013) Green hydrogen, generated via abundant renewable sources like solar, wind, and hydroelectric power, (Turner, 2004; Christoforidis et al., 2018; Zhao et al., 2021) emerges as a clean and efficient energy option with enormous potentials. Photocatalytic technology for green hydrogen has made significant progresses since the innovative work by Fujishima and Honda in water splitting on TiO_2. (Akira Fujishima and Honda, 1972) However, in typical heterogeneous photocatalytic processes, a sacrificial agent, such as triethanolamine, is crucial to consume the photo-excited hot holes and promote more hot electrons' participation in the hydrogen reduction process. (Zhang et al., 2020; Zhang et al., 2021) Unfortunately, the non-selective oxidation of sacrificial agents to by-products like CO_2 severely increases the energy consumption in photocatalysis.

Photoreforming process of biomass emerges as an intriguing alternation to utilize photoinduced holes to reform biomass and produce valuable chemical fuels while generate hydrogen through the reduction of protons from water by electrons. (Sanwald et al., 2017; Kuehnel and Reisner, 2018; Kawai and Sakata, 1980) Achieving highly efficient photoreforming of biomass holds the key to the high-value utilization of biomass and the scalable production of green hydrogen, addressing issues in environmental deterioration and energy crises. However, the fledgling yet promising field lacks highly active and selective photocatalysts with a strong full-spectrum sunlight harvesting efficiency.

Recent advancements in two-dimensional (2D) semiconductors have shown a great promise in supporting a range of photocatalytic processes due to their high charge mobility and exclusive optical properties. (Hou et al., 2013) Among these, $ZnIn_2S_4$ (ZIS), a ternary metal chalcogenide, exhibits fascinating performances in the photocatalytic reforming process of biomass due to its distinct physiochemical properties, such as wide-ranging light absorption and controllable bandgap energy. (Wu et al., 2021; Pan et al., 2018; Wang et al., 2018; Zhang et al., 2016) Nonetheless, ZIS faces limitations like fast recombination and fatigue movement of photoexcited charge carriers, as well as instability and toxicity, hindering its large-scale applications. (Pan et al., 2018; Wang et al., 2021) To overcome these challenges, the decoration of ZIS through the fabrication of heterojunctions, such as ZnO@ZIS, (Zhang et al., 2023a) CdS@ZIS, (Liu et al., 2022) and $Ti_3C_2T_x$/ZIS, (Hou et al.,

* Corresponding authors.
E-mail addresses: jinqiang.zhang@adelaide.edu.au (J. Zhang), shaobin.wang@adelaide.edu.au (S. Wang), hongqi.sun@uwa.edu.au (H. Sun).

https://doi.org/10.1016/j.ces.2023.119532
Received 25 August 2023; Received in revised form 15 October 2023; Accepted 14 November 2023
Available online 19 November 2023

2022) can enhance charge kinetics and direct charge mobility pathways. In heterojunction photocatalysts, charge separation occurs easily due to the interfacial internal electric field (IEF) resulting from the different work functions of each counterpart. (Zhang et al., 2023b) The separated hot carriers migrate to the catalyst surface for outputs based on the direction and magnitude of the driving force and the transferring pathway (i.e., the distance between the interface and surface). Therefore, optimizing the interfacial IEF and shortening the charge transferring distance are crucial in facilitating the rapid participation of electron-hole pairs in redox reactions. Compared to heterojunctions with random interfaces, the greater contact area of 2D/2D Van der Waals (VDW) heterojunctions provides giant and quick charge transferring channels at the interfacial junction. (Zhang et al., 2023c) Additionally, 2D nanosheets take advantage of their ultra-thin nanostructure, boosting the mobility and promoting the transfer of more hot carriers into chemical processes. Thus, seeking a promising 2D semiconductor material to hybridize ZIS into 2D/2D VDW heterojunctions is highly important to maximizing charge dynamics for intensified photocatalytic performances.

Graphitic carbon nitride (CN), a classic 2D metal-free polymeric photocatalytic nanomaterial, has drawn plenty of attention because of its narrow bandgap energy (2.7 eV), non-toxicity, and excellent absorption in the visible light region. (Bhunia et al., 2014; She et al., 2017) Moreover, the nanosheet structure of CN makes it an interesting candidate for photocatalytic reactions. (Ong et al., 2016) Although this promising material still has its own limitations, such as low electronic conductivity, weak near-infrared light response, and sluggish charge dynamics, especially lacking active sites/hot spots for biomass photoreforming, its hybridization with ZIS not only rejuvenates the fatigue hot carriers, but also effectively reduces the catalyst cost and the potential for secondary contamination. Since the morphology and band structure of carbon nitride vary with the precursor, how different types of carbon nitride affect the charge separation mechanism and diffusion pathway in ZIS/CN heterojunction is rarely reported, which is highly important to develop efficient heterostructure photocatalysts.

As such, this work focused on synthesizing a 2D/2D ZIS/CN VDW heterojunction by an electrostatic self-assembly strategy and maximizing the dynamics of photo-excited charge carriers for robust hydrogen production in biomass photoreforming. Results revealed that both the interfacial IEF and the transferring distance of hot carriers collectively determined the charge dynamics. Tailoring the transferring mechanism and shortening the mobility pathway of hot carriers in the heterojunction realized their fast outputs for redox reactions. Glucose, a sugar aldose and basic unit of cellulose, was chosen for evaluating the photocatalytic performance of the VDW heterojunction in H_2 generation from glucose photoreforming, and an optimal throughput with less ZIS involvement on the 2D/2D ZIS/CN VDW heterojunction was achieved. Investigations of band structure and diffusion pathway of hot carriers led to a well-defined catalyst design principle for robust photoreforming of glucose. The work is expected to unveil the crucial factors of VDW heterojunctions in determining charge dynamics, and advance catalyst modification strategy, contributing to the development of more robust photocatalysts for solar light harvesting, highly valuable biomass utilization, and green hydrogen production.

2. Methods

2.1. Preparation of CN

CN with a bulk structure was synthesized using melamine as the precursor, which was directly polymerized in a muffle furnace at 550 °C for 2 h. For CN nanosheets, dicyanamide or urea was used as the precursor using the same polymerization method. The resulting nanomaterials were named MCN (melamine as precursor), DCN (dicyanamide as precursor), and UCN (urea as precursor).

2.2. Preparation of ZIS nanosheets

ZIS was synthesized via a one-pot hydrothermal approach. Specifically, 0.18 g of $InCl_3$, 0.12 g of TAA and 0.08 g of $Zn(CH_3COO)_2{\cdot}2H_2O$ were mixed in a solution containing 15 mL of ultra-pure water and 15 mL of anhydrous ethanol, with 30 min of intense stirring. The mixture was then heated at 180 °C for 24 h in a sealed Teflon-lined autoclave. The resulting yellow powders were collected, washed with anhydrous ethanol and ultra-pure water, and dried in a vacuum oven at 50 °C overnight.

2.3. Preparation of ZIS/CN heterojunctions

2D/2D ZIS/CN (e.g., ZIS/MCN, ZIS/DCN and ZIS/UCN) VDW heterojunctions were fabricated using an electrostatic self-assembly strategy. In detail, 80 mg of ZIS and 200 mg of CN (e.g., MCN, DCN and UCN) were dispersed in a solution of absolute ethanol and ultra-pure water through ultrasonication and stirring. The solution was sealed in a Teflon-lined autoclave and heated at 120 °C for 12 h. The resulting yellowish solid was washed with anhydrous ethanol and ultra-pure water, then dried in a vacuum oven overnight, resulting in ZIS/MCN, ZIS/DCN, and ZIS/UCN heterojunctions.

3. Results and discussions

3.1. Catalyst preparation and characterizations

2D/2D ZIS/CN VDW heterojunctions were synthesized by stacking ZIS on the surface of CN using an electrostatic self-assembly strategy. To tailor the charge dynamics, including charge separation and accumulation, different types of carbon nitride with varying morphologies and band structures were acquired to hybridize with ZIS for the formation of 2D/2D ZIS/CN VDW heterojunctions. As depicted in Fig. 1, MCN with a bulk nanostructure was synthesized through the calcination of melamine at 550 °C, while dicyandiamide and urea were used as precursors for preparing DCN and UCN, respectively, resulting in the lamellar nanostructures. Subsequently, 2D ZIS nanoplates were stacked on the carbon nitrides with varying morphologies and band structures through a hydrothermal process.

Transmission electron microscopy (TEM) images provided insights into the morphology of various types of carbon nitride and ZIS/DCN VDW heterojunctions. As shown in Fig. S1, MCN exhibited micron-sized block structures (Fig. S1a), while veil-like ultrathin nanosheets were observed on DCN and UCN samples (Fig. S1b and c). Besides, ZIS displayed a well-defined 2D hexagonal lamina nanostructure (Fig. 2a). Consequently, upon the electrostatic self-assembly of ZIS and CN, a layer-by-layer nanostructure was obtained in ZIS/DCN heterojunction (Fig. 2b). High-resolution transmission electron microscopy (HRTEM) of ZIS/DCN revealed an interplanar crystal spacing of 0.32 nm (Fig. 2c), matching well with the (1 0 2) facet of ZIS. Additionally, amorphous carbon nitride regions were observed. In particular, EDX elemental mapping images indicated that ZIS with smaller nanosheets were tightly and uniformly attached to the surface of 2D DCN (Fig. 2d – i and Figs. S2 and S3). Consequently, a 2D/2D ZIS/DCN VDW heterojunction with large contacts and strong interfacial interactions was successfully prepared.

Thermogravimetric (TG) analysis was carried out to evaluate the mass loss of three ZIS/CN VDW heterojunctions in the temperature range of 30–1000 °C with a heating rate of 10 ℃ min^{-1} (Cai et al., 2021) under nitrogen atmosphere (Fig. S4). When the temperature reaches above 500 °C, TG curves revealed that the three types of ZIS/CN VDW heterojunctions start to decompose. CN would not completely decompose until the temperature exceeded 700° C. Therefore, the total mass losses of ZIS/DCN, ZIS/MCN, and ZIS/UCN reached 65.9, 68.7, and 70.2 %, respectively, before 700° C, which were close to the theoretical content of carbon nitride in the heterojunctions (71.4 %). X-ray

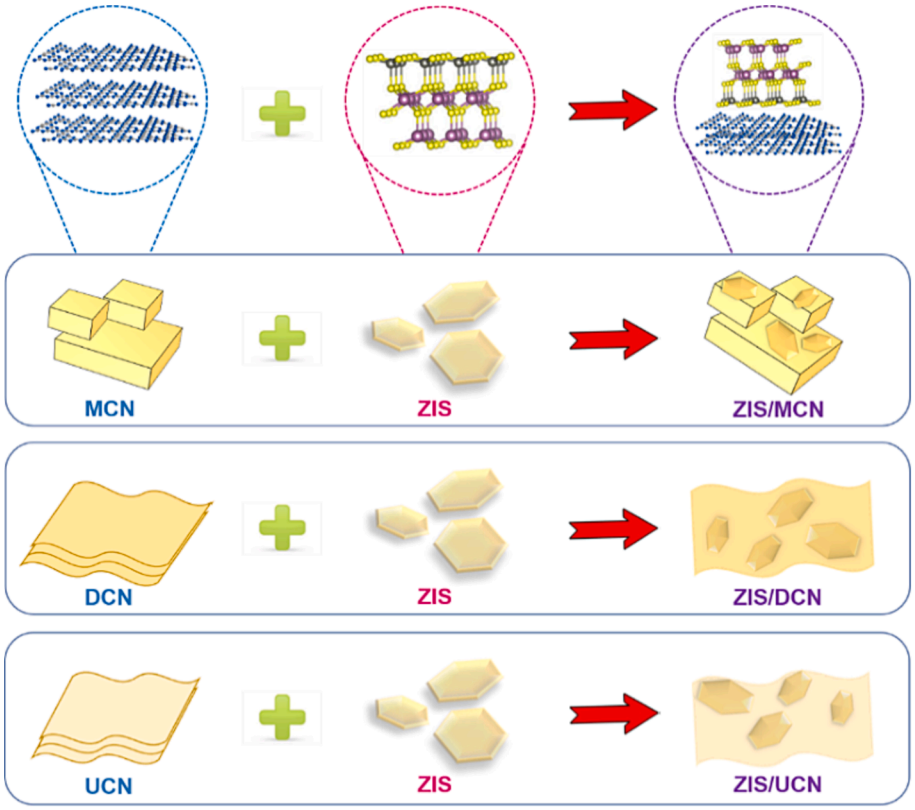

Fig. 1. Synthesis of different types of 2D/2D ZIS/CN VDW heterojunction.

diffraction (XRD) patterns were collected to analyze the crystal structure of CN materials, ZIS and their heterojunctions (Fig. S5). In the CN samples, two prominent characteristic peaks were observed at 13.1° and 27.3°. The former (100) peak corresponds to the interplanar tri-s-triazine units with a periodic structure, (Ou et al., 2017) while the latter (002) peak represents the interlayer stacking of conjugated aromatic structures. (Wang et al., 2009; Cao et al., 2015) It is worth noting that the intensity of the (002) peak was reduced in DCN and UCN compared to MCN, indicating the thinner nanosheets of DCN and UCN, and the bulk structure of MCN. Besides, the XRD pattern for ZIS exhibited distinct peaks at 21.6°, 27.5°, 30.4°, 39.8°, 47.1°, 52.5° and 55.5°, which correspond to (006), (102), (104), (108), (110), (116) and (202) crystallographic planes of hexagonal ZIS, respectively (JCPDS file No. 72–0773). (Du et al., 2019) Following the fabrication of the ZIS/CN heterojunction, a characteristic diffraction peak at 27.4° corresponding to the overlap of the (002) peak of CN and the (102) facet of ZIS was observed. Additionally, the other characteristic diffraction peaks assigned to ZIS were also present, providing the evidence for the successful formation of the ZIS/CN heterojunction.

FT-IR spectra were obtained to explore the functional groups present in ZIS, CN samples and their heterojunctions (Fig. 3a). Prominent characteristic peaks for CN samples were identified, including N-H and O-H stretching vibrations in the range of 3100 to 3500 cm^{-1} and C_6N_7 unit at 1229, 1327, 1428, 1566 and 1633 cm^{-1}. (Tian et al., 2022) Besides, the characteristic peak at 808 cm^{-1} is ascribed to the triazine unit of carbon nitride materials. (Pan et al., 2019) Notably, no distinctive stretch modes were observed between pristine CN and their hybridizations with ZIS, as no characteristic peaks were evident on the ZIS material. This suggests that the ZIS/CN composites retain similar skeletons to pristine CN samples, indicating that the loading of ZIS nanosheets on the carbon nitride host did not disrupt the molecular structure of CN materials.

Near-edge X-ray absorption fine structure (NEXAFS) spectroscopy was collected to confirm the formation of ZIS/CN heterojunctions. In the C-K edge spectra (Fig. 3b), peaks at 287.8 and 288.2 eV were assigned to the C–C and C–N-C resonances, respectively, within the CN framework of carbon nitride materials. Meanwhile, all CN and ZIS/CN samples displayed two typical peaks, which are respectively at 399 and 402 eV, in the N-K edge spectra (Fig. 3c). The first is from the C-N-C coordination in CN units and the latter is corresponding to the N-3C bridging among three tri-s-triazine rings. Additionally, ZIS and ZIS/CN samples exhibited two main characteristic peaks at 2465 and 2469 eV, attributed to the S atom with low-coordination and S^{2-}, respectively (Fig. 3d). Peak intensities in C-K and N-K edge spectra for CN and S-K edge for ZIS decreased after hybridization of ZIS with CN, confirming the formation of heterojunctions comprising of ZIS and CN.

3.2. Factors in VDW heterojunctions determining charge dynamics

The charge dynamics within the obtained heterojunction were thoroughly investigated. To gain insights into the factors influencing the charge dynamics of the heterojunction photocatalysts, the band structures of all the composite catalysts were initially proposed. UV–Vis curves of the photocatalysts were obtained to compare their light absorption abilities. A steep absorption in the range of 370 to 580 nm was observed in the prepared ZIS, and the marginal edges of CN samples were evident at around 485 nm, indicating that both pristine semiconductors were responsive to visible light. Remarkably, upon loading ZIS onto CN materials, red-shifts were observed in all the modified materials (Fig. 4a), indicating an enhanced light absorption ability in the VDW heterojunctions.

The bandgap energy of the samples was determined by the Tauc's equation: $(\alpha h\nu)^n = k(h\nu - E_g)$, where n is ½ and 2 for a direct and an indirect semiconductor, respectively. As shown in Fig. 4b and Fig. S6, the bandgap energies of MCN, DCN, UCN and ZIS were measured to be 2.60, 2.52, 2.75 and 2.34 eV, respectively. Additionally, XPS valence band (VB) spectra were acquired for all the samples to estimate the position of VB. As depicted in Fig. 4c and Fig. S7, the VB positions for

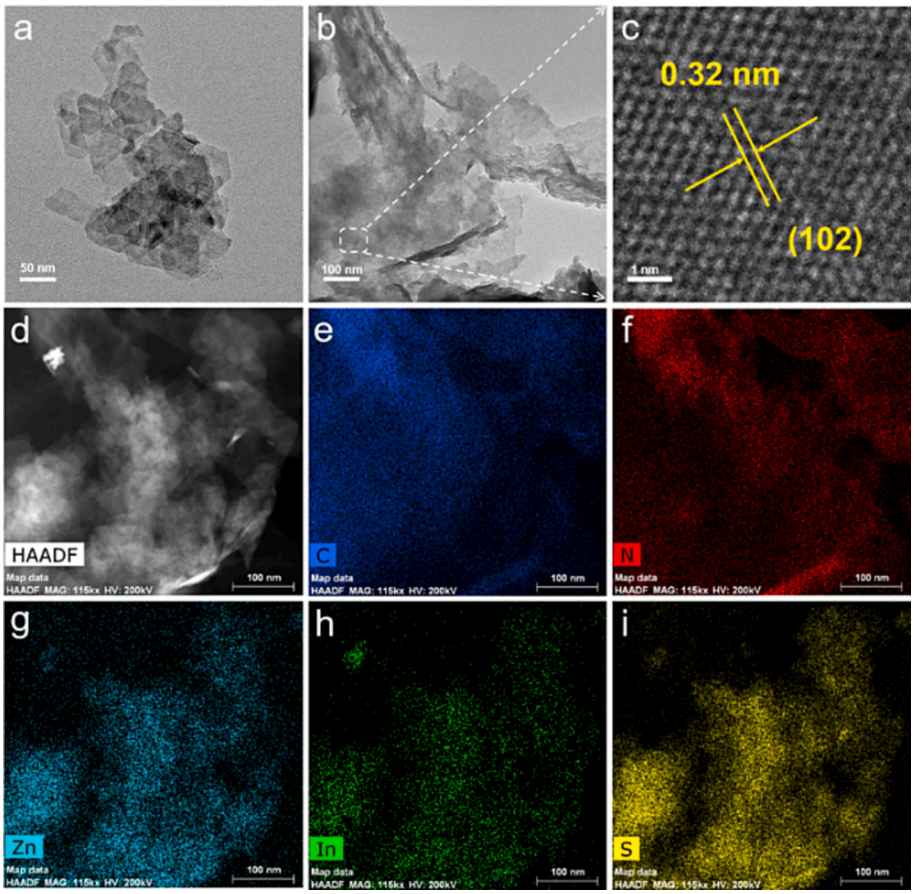

Fig. 2. Morphology observations. TEM images of (a) ZIS and (b) ZIS/DCN; (c) HRTEM image of ZIS/DCN; (d) HAADF-STEM and (e-i) STEM-EDX elemental mapping images of ZIS/DCN.

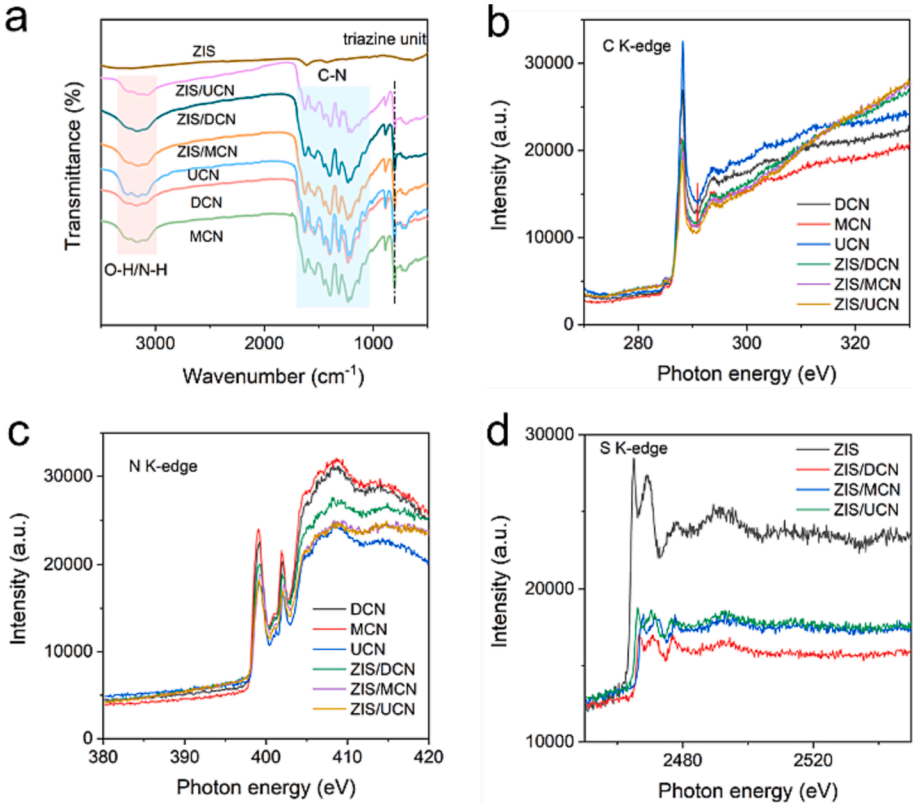

Fig. 3. Catalyst characterizations. (a) FT-IR patterns, and NEXAFS spectra, including (b) C-K edge, (c) N-K edge and (d) S-K edge, for all the prepared samples.

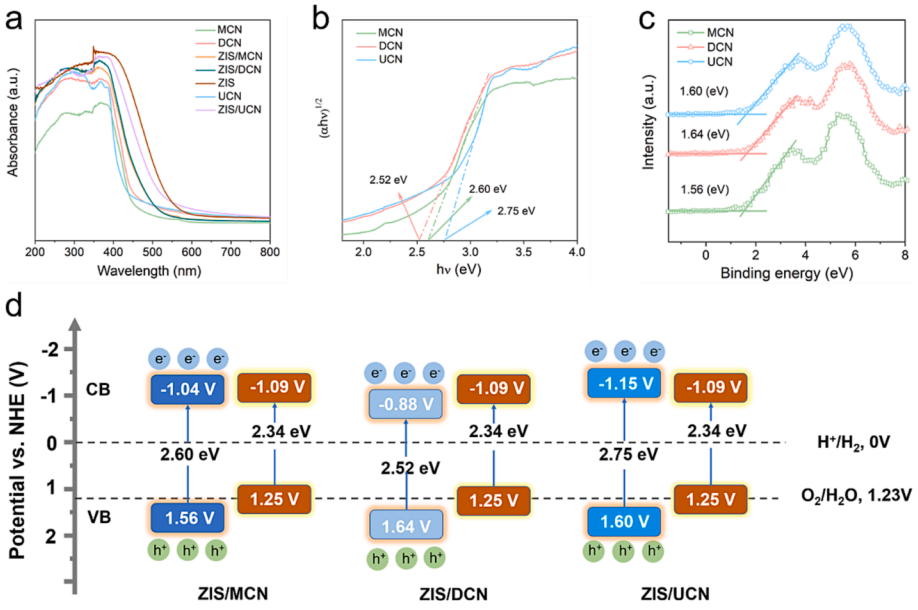

Fig. 4. Band structure investigations. (a) UV–Vis DRS spectra of all the prepared catalysts; (b) Tauc's plots for estimation of pristine CN and ZIS materials; (c) XPS valence band spectra of CN samples and (d) proposed band structures of ZIS/CN composites.

MCN, DCN, UCN and ZIS were measured to be 1.56, 1.64, 1.60 and 1.25 eV, respectively. The conduction band (E_{CB}) potential of MCN, DCN, UCN, and ZIS were obtained using the equation of $E_{CB} = E_{VB} - E_g$, which were determined to be −1.04, −0.88, −1.15, and −1.09 eV versus NHE, respectively. Mott–Schottky plots of the prepared samples were also collected at different frequencies to estimate the flat band (E_f) potential position (Fig. S8). All prepared samples show a positive slope, indicating a typical n-type semiconductor, which equals its conduction band potential. The conduction band potentials (vs Ag/AgCl) of MCN, DCN, UCN, and ZIS were measured to be −1.24, 1.08, −1.35, and −1.29 eV, respectively. Correcting $E_{Ag/AgCl}$ by 0.197 eV, the corresponding CB potentials are estimated to be approximately −1.04, −0.88, −1.15, and −1.09 eV Vs NHE, respectively. These values are consistent with the results obtained through VB-XPS calculations. These measurements confirmed the band structures for all the samples, and the results are summarized in Fig. 4d and Table S1. The band structures of ZIS/MCN and ZIS/DCN satisfy the requirements for a S-scheme charge transfer. In contrast, both the conduction band (CB) and VB of ZIS are lower than those of UCN, which is not conducive to charge separation at the interface between ZIS and UCN. Moreover, the potential difference between the CB of MCN and the VB of ZIS is lower than that between the CB of DCN and the VB of ZIS, suggesting that charge carriers would more readily be separated at the interface of ZIS/DCN compared to ZIS/MCN .

We then employed N_2 adsorption-desorption isotherms to analyze the textural properties of the heterojunction photocatalysts (Fig. 5a and b). All the prepared heterojunctions exhibited typical IV adsorption isotherms, indicative of a H3 hysteresis loop, which confirmed the presence of mesoporous structures. (Li et al., 2022) In comparison with the ZIS/DCN samples (129.4 m^2/g), the specific Brunauer-Emmett-Teller (BET) surface areas of ZIS/MCN (117.8 m^2/g) and ZIS/UCN (113.2 m^2/g) were slightly decreased, likely due to the bulk structure of MCN, and the tight contact between UCN and ZIS blocking the pores of CN samples, respectively. This was further supported by the micropores observed in the pore size distribution results, particularly in the case of the ZIS/UCN catalyst exhibiting more micropores, confirming the blocked mesopores by the tight contact within the fabricated ZIS/UCN heterostructure (Table S2). Therefore, based on the proposed band structures and the textural properties of the prepared heterojunction materials, we can conclude that ZIS/UCN exhibited weak interfacial interaction despite the tight contacts. Meanwhile, the charge dynamics in ZIS/DCN are stronger than that in ZIS/MCN, owing to the larger interfacial electric field force and shorter diffusion pathway of charge carriers in ZIS/DCN (Fig. 5c).

3.3. Interfacial IEF and charge transferring mechanism

To investigate the intrinsic electrical field and surface chemical states in the ZIS/DCN VDW heterojunction, X-ray photoelectron spectroscopy (XPS) was conducted. All the results were corrected using the C-C bond at 284.8 eV as the reference. The XPS full survey spectra displayed in Fig. S9 showed the presence of Zn, In, S, C, and N elements in the ZIS/CN samples, confirming the successful formation of the heterojunctions comprising ZIS and CN. Deconvoluted peaks at 284.8 and 288.1 eV in the C 1 s spectra were observed in CN samples, corresponding to the sp^2 C-C bond and N-C = N bond in the tri-s-triazine rings, respectively (Fig. 6a and Fig. S10a). (Zhang et al., 2016; Cao et al., 2015) Additionally, characteristic peaks at 398.3, 398.7, and 400.7 eV were fitted in the N 1 s spectra, attributed to the sp^2-bonded nitrogen (C-N = C), tertiary nitrogen N-$(C)_3$, and amino group C-N-H, respectively (Fig. 6b and Fig. S10b). (Cao et al., 2015) For the Zn 2p spectra (Figs. S10 and S11), two individual peaks at 1045.2 and 1022.1 eV corresponding to Zn $2p_{1/2}$ and Zn $2p_{3/2}$, respectively, were seen in ZIS, confirming the existence of Zn^{2+}. (Chen et al., 2015) Furthermore, the S 2p spectra could be deconvoluted into $2p_{1/2}$ and $2p_{3/2}$ peaks at 162.9 and 161.8 eV, respectively (Fig. 6c and Fig. S10c), and two peaks assigned to $3d_{3/2}$ and $3d_{5/2}$, at 452.7 eV and 445.1 eV, respectively, were found in the In 3d spectra (Fig. 6d and Fig. S10d), which are consistent with the coordination of Zn, In, and S elements in the ZIS sample.

On the other hand, all the deconvoluted peaks in C 1 s and N 1 s spectra shifted to a higher binding energy after the formation of the ZIS/DCN nanomaterial. In contrast, the characteristic peaks in the Zn 2p, In 3d, and S 2p spectra were all downshifted in ZIS/DCN compared to pristine ZIS. These results fully confirm that electron migration occurred from DCN to ZIS at the contacts in ZIS/DCN. The migration of electrons results in an IEF at the interface of ZIS/DCN, directing from ZIS to DCN. The values for work function of ZIS and DCN were also calculated by DFT simulation to go deeply into the interfacial charge transferring. As shown in Fig. S12, the work function of ZIS (5.72 eV) is lower than that of DCN (6.07 eV). The Fermi level of the corresponding ZIS (1.22 eV) is higher than that of DCN (1.57 eV), and the electrons will transfer from

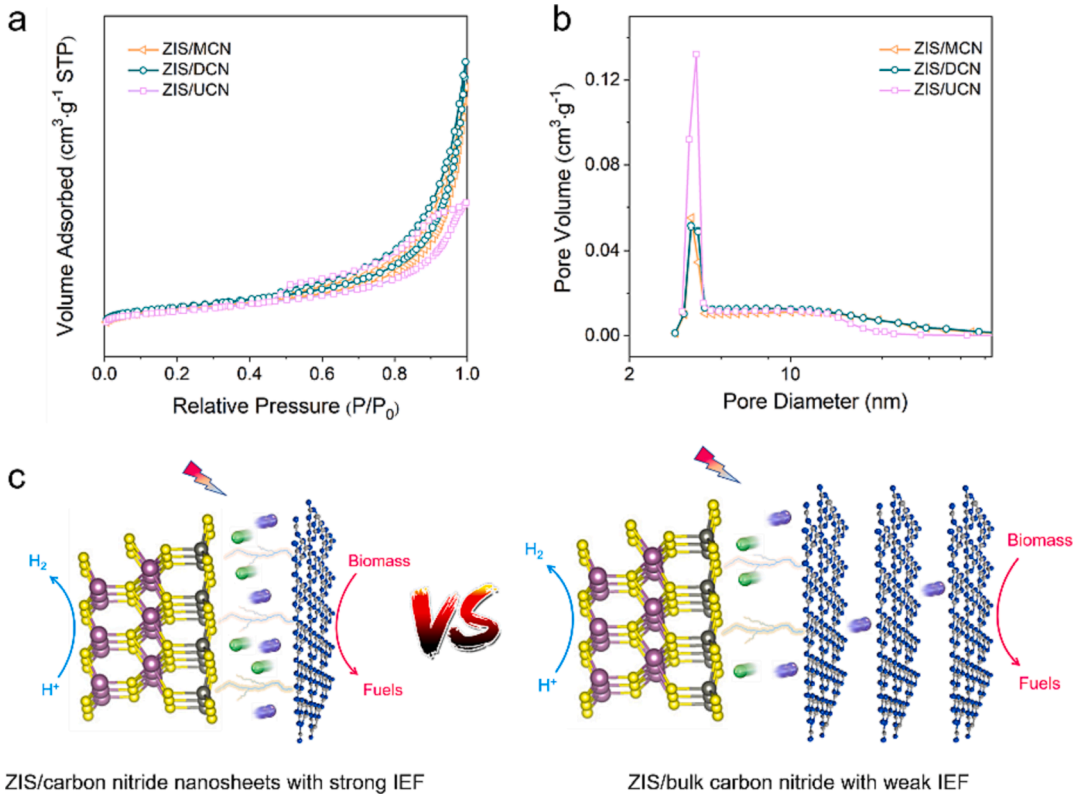

Fig. 5. (a) Nitrogen adsorption isotherms, and (b) pore size distribution of ZIS/CN heterojunctions; (c) comparison of charge dynamics in different types of ZIS/CN photocatalysts.

ZIS with a higher Fermi level to DCN with a lower Fermi level until both Fermi levels are balanced, resulting in the formation of interfacial build-in electric field pointing from ZIS to DCN. The calculation results well meet with the XPS result. Therefore, based on the bandgap energies and IEF as mentioned above, an S-type VDW heterojunction is established in the ZIS/DCN heterojunction, which significantly accelerates the mobility and hinders the recombination of charge carriers. Specifically, the photoinduced electrons at the CB of DCN migrate to the VB of ZIS for recombination, leaving hot electrons and hot holes at the CB of ZIS and VB of DCN, respectively. The separated hot electrons and hot holes then move to the surface of ZIS/DCN for the outputs into redox reactions. In situ irradiation XPS measurements were conducted to prove the S-scheme charge transferring mechanism. As displayed in Fig. 6e and Fig. S13a, peaks in C 1 s and N 1 s spectra shifted to higher binding energies. In contrast, the binding energies of peaks in In 3d and S 2p downshifted (Fig. 6f and g). These results suggest that photogenerated electrons transfer from DCN to ZIS under light irradiation, which is mainly driven by the built-in electric field pointing from ZIS towards DCN. Therefore, the in-situ irradiation XPS measurement results further demonstrate that the transferring pathway of photo-excited electron in ZIS/DCN VDW heterojunction is ascribed to a S-type mechanism.

3.4. Photoreforming performance

The optoelectronic properties of DCN and its hybridization of ZIS in ZIS/CN were studied to unveil the IEF effect on charge dynamics. Initially, fluorescence spectra of DCN and ZIS/DCN were collected to study the separation rate of photo-excited charge carriers. It can be observed from Fig. 7a that the peak intensity of ZIS/DCN was reduced when compared to DCN. A higher intensity in the PL spectra suggests a rapid recombination rate of photo-excited charge carriers. As such, the decreased peak intensity after the formation of ZIS/DCN heterojunction indicated a faster separation of charge carriers. Photoelectrochemical measurements, for example, electrochemical impedance spectroscopy (EIS) and transient photocurrents were also conducted to evaluate the charge dynamics in ZIS/CN samples. First, EIS was tested to determine the resistance of interfacial charge transport for the heterostructure samples (Fig. 7b). ZIS/DCN exhibited the lowest arc radius compared to ZIS/MCN and ZIS/UCN, indicating a low charge transfer resistance and fast charge transportation at the formed VDW interface in ZIS/DCN. Transient photocurrent (PC) response ability was also tested via an intermittent light irradiation system (Fig. 7c). ZIS/DCN exhibited a higher photocurrent density than ZIS/MCN and ZIS/UCN after the formation of the S-scheme VDW heterojunction. This trend is consistent with that in the EIS spectra, indicating an accelerated charge separation rate in ZIS/DCN due to the interfacial interaction. Moreover, a good reproducibility can be clearly seen, suggesting a satisfactory photostability of the novel S-scheme VDW heterojunction.

The performances of all obtained materials were tested in a visible light-driven photoreforming process using D-+-glucose as a model biomass. Before the performance evaluation, the effect of glucose concentration (48, 96, and 144 ppm) on hydrogen evolution was assessed, showing that 96 ppm of glucose solution was the best substrate candidate for the photoreforming of glucose (Fig. 7d). Then the photoreforming activity of all the prepared samples in the reforming of glucose was studied. As exhibited in Fig. 7e, pristine CN samples prepared with different precursors exhibited negligible activity in the photoreforming of glucose, indicating the sluggish charge dynamics in CN samples for photoreforming of glucose. However, after the loading of ZIS on the surface of CN samples, all the ZIS/CN VDW heterojunctions exhibited intensified hydrogen evolution, as ZIS provided an impressive hydrogen production rate of 1036.86 μmol g^{-1} in a 3-h photo-reaction. The photoreforming performance of ZIS/DCN was almost 350 times higher than that of pristine DCN, showing a remarkable enhancement in harvesting solar energy to generate green hydrogen. As such, the hydrogen production performance per unit mass of ZIS was compared

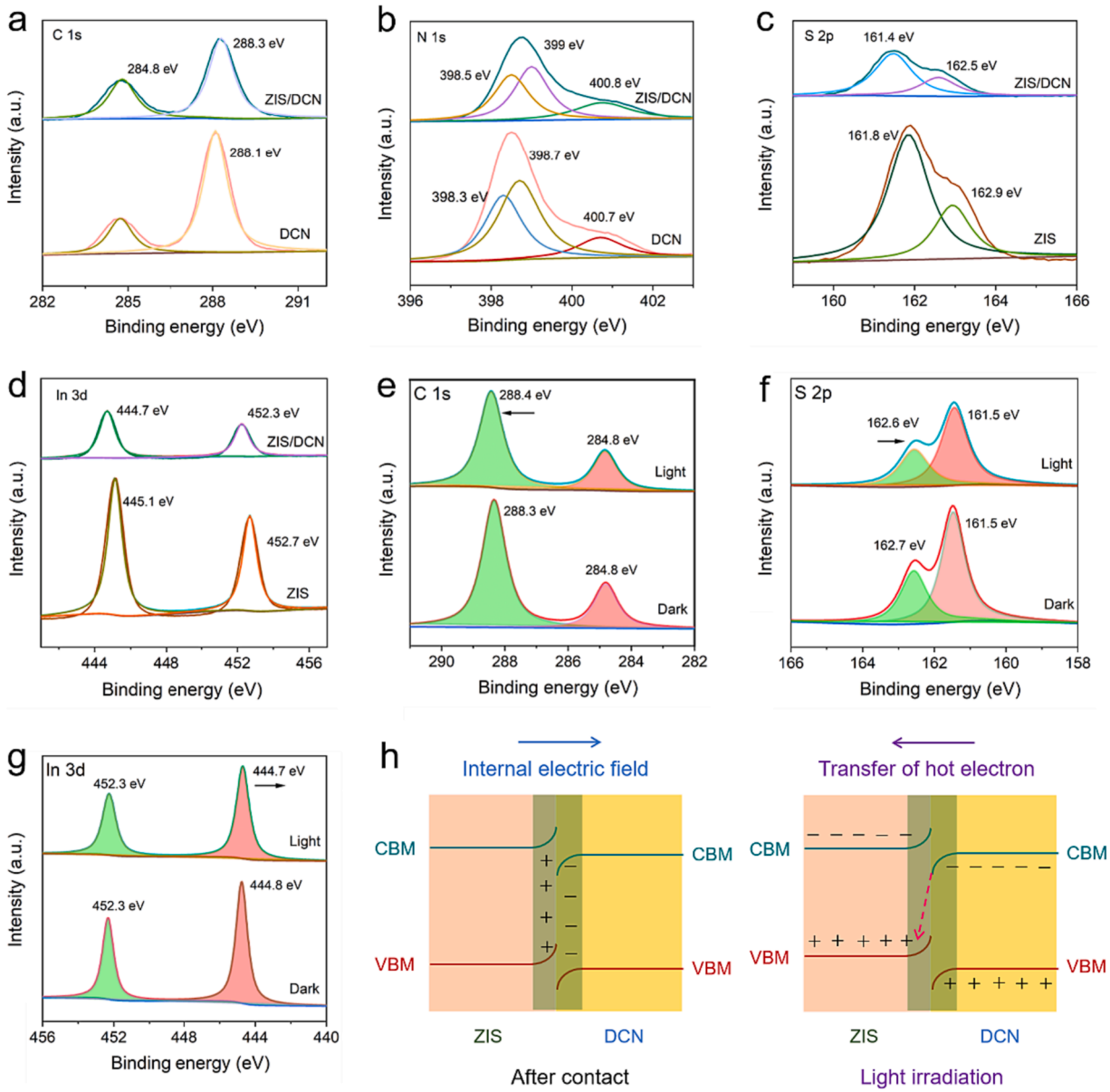

Fig. 6. XPS spectra including (a) C 1 s, (b) N 1 s, (c) S 2p and (d) In 3d; In situ light irradiation XPS spectra including (e) C 1 s, (f) S 2p, (g) In 3d and (h) interfacial internal electric field within ZIS/DCN VDW heterojunction.

between ZIS/DCN and pristine ZIS. As exhibited in Fig. 7f, the highest H_2 production was achieved on ZIS/DCN (1193.75 μmol g_{ZIS}^{-1}) among all prepared samples. Considering the low performance of carbon nitride in the photoreforming process, the higher hydrogen generation rate of ZIS/DCN than ZIS manifested the significant role of interfacial IEF in enhancing the charge dynamics and increasing photocatalytic throughputs. Additionally, after loading ZIS on a low cost and environmental benign support of carbon nitride, the photocatalytic activity of ZIS was significantly improved, offering a cost-effective photocatalyst and another avenue for catalyst modification.

The photocatalytic green hydrogen production from glucose reforming process on different types of ZIS/CN samples was also compared (Fig. 7e). When ZIS was loaded on the host of UCN nanosheets, the type-I heterojunction failed to accelerate the separation of charge carriers and improve charge dynamics, despite the tight contacts and short transferring pathway of charge carriers after separation. As a result, the hydrogen generation rate was the lowest among the three types of heterojunctions. Meanwhile, when ZIS was coated on the surface of MCN and DCN, both S-scheme charge transfer mechanisms were obtained at the interface of heterojunctions. However, the photocatalytic hydrogen generation capability of ZIS/MCN was lower than that of ZIS/DCN. On one aspect, the bulk structure of MCN is not conducive to efficiently transferring hot carriers to the surface of the photocatalyst. On the other hand, the oxidation potential of ZIS/MCN is lower than that of ZIS/DCN after charge separation, collectively determining the highest hydrogen production on ZIS/DCN VDW heterojunction.

3.5. Reaction mechanism

The mechanism of photoreforming of glucose over the Z-scheme ZIS/DCN VDW heterojunction was proposed and displayed in Fig. 8. Typically, ZIS and DCN can be simultaneously excited by sunlight to release photoinduced electrons from the VB to the CB. The photoinduced electrons at the CB of DCN migrate to the VB of ZIS for recombination, leaving photoinduced electrons and holes at the CB of ZIS and VB of DCN, respectively, to achieve efficient charge separation. The hot electrons transfer across the ZIS nanosheet, accumulating on the surface of

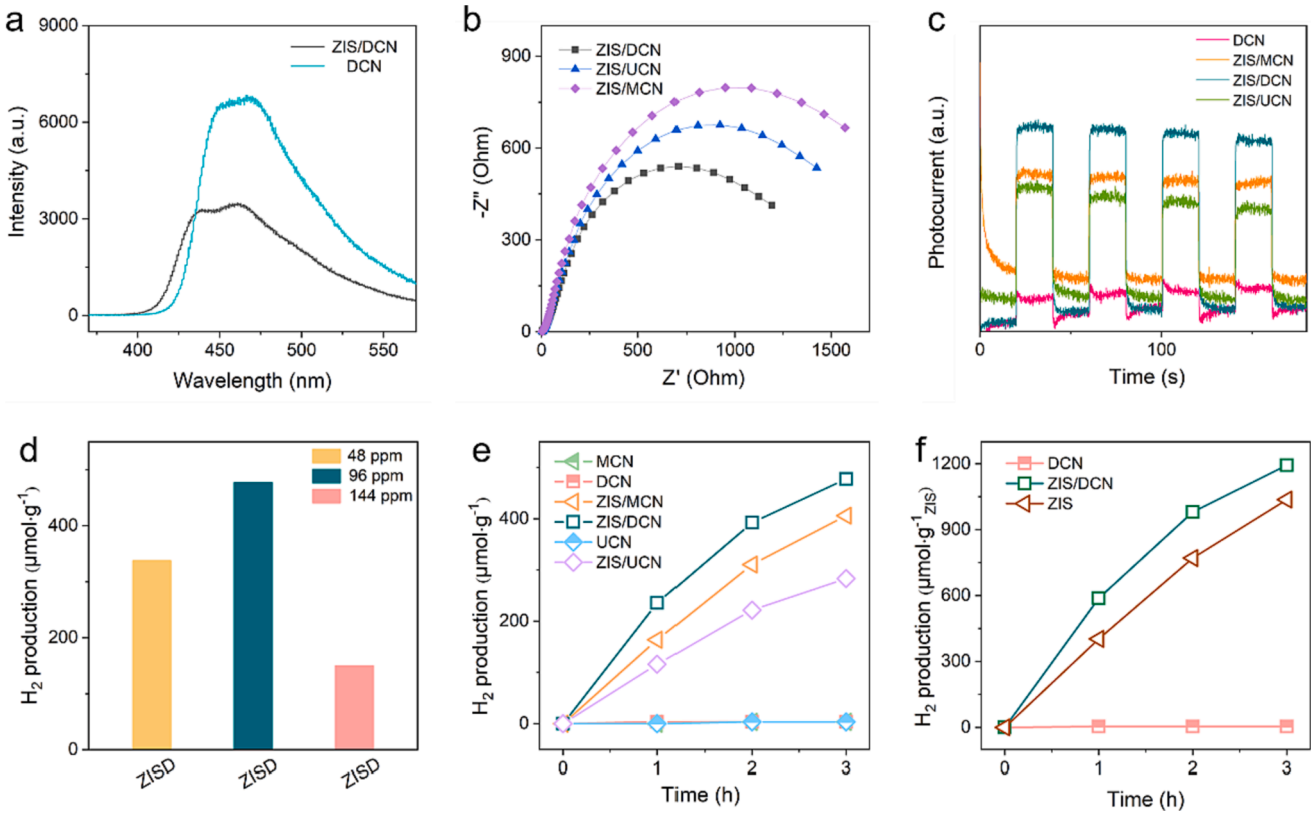

Fig. 7. (a) PL spectra of DCN and ZIS/DCN samples, (b) EIS spectra and (c) photocurrent results of ZIS/CN samples; (d) effect of glucose concentration on hydrogen generation in photoreforming of glucose over ZIS/DCN; (e) hydrogen generation in photoreforming of glucose on CN and ZIS/CN samples; (f) hydrogen generation per unit mass of ZIS in photoreforming of glucose.

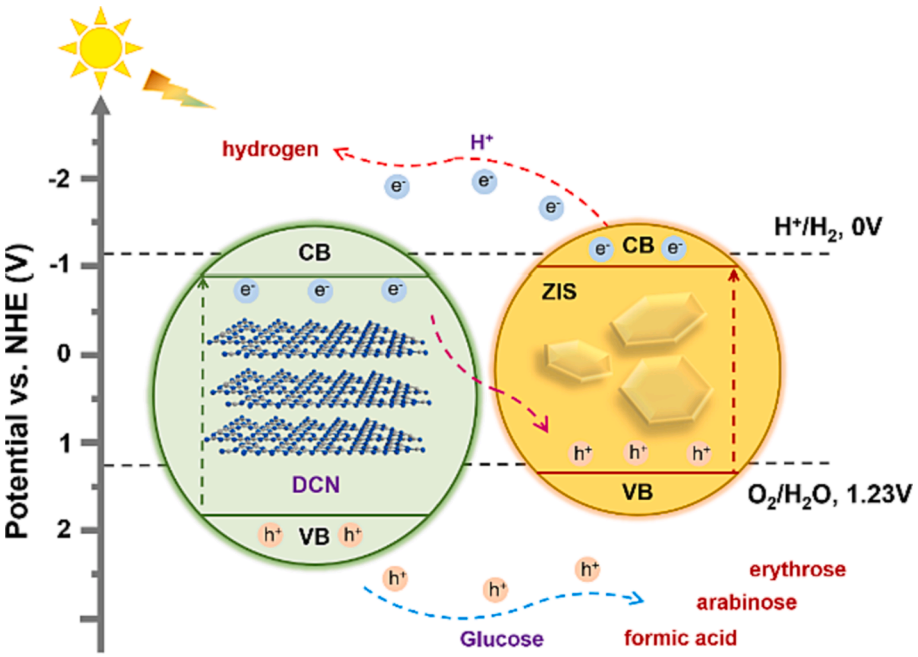

Fig. 8. Reaction mechanism of photoreforming of glucose on ZIS/DCN.

ZIS for hydrogen reduction, while the photo-generated hot holes move to the surface of DCN to oxidize glucose into a series of products, including arabinose, erythrose, and formic acid. (Chong et al., 2014; Bellardita et al., 2018) Therefore, the functionality-performance relationship of heterojunction photocatalysts becomes apparent: Hot carriers are the main driving force in the photoreforming of biomass, and thus, charge dynamics are the key to the output of hot carriers for redox reactions. In a VDW heterojunction, two factors, e.g., the interfacial IEF and subsequent diffusion pathway, determine the activity of charge carriers. As a result, maximizing interfacial interaction for fast

charge separation and minimizing the transferring distance of hot carriers for rapid outputs would achieve higher photocatalytic throughputs.

4. Conclusions

In summary, we successfully loaded ZIS, a 2D ternary chalcogenide, onto the surface of 2D CN nanosheets, creating 2D/2D VDW heterojunctions. Among all the prepared catalysts, ZIS/DCN exhibited the highest performance in H_2 generation, achieving a rate of 1193.75 μmol g_{ZIS}^{-1} under a 3-h light irradiation. This rate surpassed that of both ZIS and CN, making it a promising, cost-effective, and environmentally benign photocatalyst for biomass reforming. The reaction mechanism behind this success was unveiled, wherein a S-scheme charge transfer enabled the faster charge separation, and the ultrathin nanostructure provided a short charge diffusion pathway for efficient outputs. Additionally, the catalyst design principle was discussed, in which an enlarged interfacial IEF and a shortened charge diffusion pathway are highly desirable to realize the maximum charge dynamics and photocatalytic performances. This work elucidates the key factors in VDW heterojunctions in determining the charge dynamics and photocatalysis, which is beneficial for developing more cost-effective photocatalysts for harvesting sunlight and valuable utilisation of biomass energy resources.

Declaration of competing interest

The authors declare that they have no known competing financial interests or personal relationships that could have appeared to influence the work reported in this paper.

Data availability

Data will be made available on request.

Acknowledgement

This work was supported by the Australian Research Council (DP200103206).

Appendix A. Supplementary data

Supplementary data to this article can be found online at https://doi.org/10.1016/j.ces.2023.119532.

References

Akira Fujishima, Honda K., Electrochemical photolysis of water at a semiconductor electrode. *Nature* **1972**, *238*, 37-38.

Bellardita, M., García-López, E.I., Marcì, G., Nasillo, G., Palmisano, L., 2018. Photocatalytic solar light H_2 production by aqueous glucose reforming. Eur. J. Inorg. Chem. 2018 (41), 4522–4532.

Bhunia, M.K., Yamauchi, K., Takanabe, K., 2014. Harvesting solar light with crystalline carbon nitrides for efficient photocatalytic hydrogen evolution. Angew. Chem. Int. Ed. 53 (41), 11001–11005.

Cai, M., Wu, Z., Li, Z., Wang, L., Sun, W., Tountas, A.A., Li, C., Wang, S., Feng, K., Xu, A.-B., Tang, S., Tavasoli, A., Peng, M., Liu, W., Helmy, A.S., He, L., Ozin, G.A., Zhang, X., 2021. Greenhouse-inspired supra-photothermal CO_2 catalysis. Nat. Energy 6 (8), 807–814.

Cao, S., Low, J., Yu, J., Jaroniec, M., 2015. Polymeric photocatalysts based on graphitic carbon nitride. Adv. Mater. 27 (13), 2150–2176.

Chen, W., Liu, T.Y., Huang, T., Liu, X.H., Zhu, J.W., Duan, G.R., Yang, X.J., 2015. One-pot hydrothermal route to synthesize the $ZnIn_2S_4$/g-C_3N_4 composites with enhanced photocatalytic activity. J. Mater. Sci. 50 (24), 8142–8152.

Chong, R., Li, J., Ma, Y., Zhang, B., Han, H., Li, C., 2014. Selective conversion of aqueous glucose to value-added sugar aldose on TiO_2-based photocatalysts. J. Catal. 314, 101–108.

Christoforidis, K.C., Syrgiannis, Z., La Parola, V., Montini, T., Petit, C., Stathatos, E., Godin, R., Durrant, J.R., Prato, M., Fornasiero, P., 2018. Metal-free dual-phase full organic carbon nanotubes/g-C_3N_4 heteroarchitectures for photocatalytic hydrogen production. Nano Energy 50, 468–478.

Du, C., Zhang, Q., Lin, Z., Yan, B., Xia, C., Yang, G., 2019. Half-unit-cell $ZnIn_2S_4$ monolayer with sulfur vacancies for photocatalytic hydrogen evolution. Appl. Catal. B-Environ. 248, 193–201.

Hou, Y., Laursen, A.B., Zhang, J., Zhang, G., Zhu, Y., Wang, X., Dahl, S., Chorkendorff, I., 2013. Layered nanojunctions for hydrogen-evolution catalysis. Angew. Chem. Int. Ed. 52 (13), 3621–3625.

Hou, S., Xu, C., Ju, X., Jin, Y., 2022. Interfacial assembly of $Ti_3C_2T_x$/$ZnIn_2S_4$ heterojunction for high-performance photodetectors. Adv. Sci. 9 (35), e2204687.

Kawai, T., Sakata, T., 1980. Conversion of carbohydrate into hydrogen fuel by a photocatalytic process. Nature 286 (5772), 474–476.

Kuehnel, M.F., Reisner, E., 2018. Solar hydrogen generation from lignocellulose. Angew. Chem. Int. Ed. 57 (13), 3290–3296.

Li, L., Ma, D., Xu, Q., Huang, S., 2022. Constructing hierarchical $ZnIn_2S_4$/g-C_3N_4 S-scheme heterojunction for boosted CO_2 photoreduction performance. Chem. Eng. J. 437, 135153.

Liu, X., Xu, J., Jiang, Y., Du, Y., Zhang, J., Lin, K., 2022. In-situ construction of CdS@ZIS Z-scheme heterojunction with core-shell structure: Defect engineering, enhance photocatalytic hydrogen evolution and inhibit photo-corrosion. Int. J. Hydrog. Energy 47 (83), 35241–35253.

Ong, W.-J., Tan, L.-L., Ng, Y.H., Yong, S.-T., Chai, S.-P., 2016. Graphitic carbon nitride (g-C3N4)-based photocatalysts for artificial photosynthesis and environmental remediation: Are we a step closer to achieving sustainability? Chem. Rev. 116 (12), 7159–7329.

Ou, H., Lin, L., Zheng, Y., Yang, P., Fang, Y., Wang, X., 2017. Tri-s-triazine-based crystalline carbon nitride nanosheets for an improved hydrogen evolution. Adv. Mater. 29 (22), 1700008.

Pan, X., Shang, C., Chen, Z., Jin, M., Zhang, Y., Zhang, Z., Wang, X., Zhou, G., 2019. Enhanced photocatalytic H_2 evolution over $ZnIn_2S_4$ flower-like microspheres doped with black phosphorus quantum dots. Nanomaterials 9 (9), 1266.

Pan, Y., Yuan, X., Jiang, L., Yu, H., Zhang, J., Wang, H., Guan, R., Zeng, G., 2018. Recent advances in synthesis, modification and photocatalytic applications of micro/nano-structured zinc indium sulfide. Chem. Eng. J. 354, 407–431.

Sanwald, K.E., Berto, T.F., Eisenreich, W., Jentys, A., Gutiérrez, O.Y., Lercher, J.A., 2017. Overcoming the rate-limiting reaction during photoreforming of sugar aldoses for H_2-generation. ACS Catal. 7 (5), 3236–3244.

She, X., Wu, J., Xu, H., Zhong, J., Wang, Y., Song, Y., Nie, K., Liu, Y., Yang, Y., Rodrigues, M.-T.-F., Vajtai, R., Lou, J., Du, D., Li, H., Ajayan, P.M., 2017. High efficiency photocatalytic water splitting using 2D α-Fe_2O_3/g-C_3N_4 Z-scheme catalysts. Adv. Energy Mater. 7 (17), 1700025.

Sun, H., Zhou, G., Liu, S., Ang, H.M., Tadé, M.O., Wang, S., 2013. Visible light responsive titania photocatalysts codoped by nitrogen and metal (Fe, Ni, Ag, or Pt) for remediation of aqueous pollutants. Chem. Eng. J. 231, 18–25.

Tian, S., Ren, H., Liu, Z., Miao, Z., Tian, L., Li, J., Liu, Y., Wei, S., Wang, P., 2022. ZnS/g-C_3N_4 heterojunction with Zn-vacancy for efficient hydrogen evolution in water splitting driven by visible light. Catal. Commun. 164, 106422.

Turner, J.A., 2004. Sustainable hydrogen production. Science 305 (5686), 972–974.

Wang, S., Guan, B.Y., Wang, X., Lou, X.W.D., 2018. Formation of hierarchical Co_9S_8@$ZnIn_2S_4$ heterostructured cages as an efficient photocatalyst for hydrogen evolution. J. Am. Chem. Soc. 140 (45), 15145–15148.

Wang, X., Maeda, K., Thomas, A., Takanabe, K., Xin, G., Carlsson, J.M., Domen, K., Antonietti, M., 2009. A metal-free polymeric photocatalyst for hydrogen production from water under visible light. Nat. Mater. 8 (1), 76–80.

Wang, J., Sun, S., Zhou, R., Li, Y., He, Z., Ding, H., Chen, D., Ao, W., 2021. A review: Synthesis, modification and photocatalytic applications of $ZnIn_2S_4$. J. Mater. Sci. Technol. 78, 1–19.

Wu, X., Xie, S., Zhang, H., Zhang, Q., Sels, B.F., Wang, Y., 2021. Metal sulfide photocatalysts for lignocellulose valorization. Adv. Mater. 33 (50), 2007129.

Zhang, J., Li, Y., Zhao, X., Zhang, H., Wang, L., Chen, H., Wang, S., Xu, X., Shi, L., Zhang, L.C., Veder, J.P., Zhao, S., Nealon, G., Wu, M., Wang, S., Sun, H., 2020. A hydrogen-initiated chemical epitaxial growth strategy for in-plane heterostructured photocatalyst. ACS Nano 14, 17505–17514.

Zhang, J., Li, Y., Zhao, X., Wang, L., Chen, H., Wang, S., Xu, X., Shi, L., Zhang, L.-C., Zhu, Y., Zhang, H., Liu, Y., Nealon, G., Zhang, S., Wu, M., Wang, S., Sun, H., 2021. Aligning potential differences within carbon nitride based photocatalysis for efficient solar energy harvesting. Nano Energy 89, 106357.

Zhang, Z., Liu, K., Feng, Z., Bao, Y., Dong, B., 2016. Hierarchical sheet-on-sheet $ZnIn_2S_4$/g-C_3N_4 heterostructure with highly efficient photocatalytic H_2 production based on photoinduced interfacial charge transfer. Sci. Rep. 6 (1), 19221.

Zhang, J., Zhao, X., Chen, L., Li, S., Chen, H., Zhu, Y., Wang, S., Liu, Y., Zhang, H., Duan, X., Wu, M., Wang, S., Sun, H., 2023a. Intrinsic mechanisms of morphological engineering and carbon doping for improved photocatalysis of 2D/2D carbon nitride Van der Waals heterojunction. Energy Environ. Mater. 6, e12365.

Zhang, J., Tan, X., Shi, L., Chen, H., Liu, Y., Wang, S., Duan, X., Wu, M., Sun, H., Wang, S., 2023b. Tandem internal electric fields in intralayer/interlayer carbon nitride homojunction with a directed flow of photo-excited electrons for photocatalysis. Appl. Catal. b: Environ. 333, 122781.

Zhang, Y., Xu, M., Zhou, W., Song, X., Liu, X., Zhang, J., Chen, S., Huo, P., 2023c. Fabricated ZnO@$ZnIn_2S_4$ S-scheme heterojunction photocatalyst for enhanced electron-transfer and CO_2 reduction. J. Colloid Interface Sci. 650 (Pt B), 1762–1772.

Zhao, D., Wang, Y., Dong, C.-L., Huang, Y.-C., Chen, J., Xue, F., Shen, S., Guo, L., 2021. Boron-doped nitrogen-deficient carbon nitride-based Z-scheme heterostructures for photocatalytic overall water splitting. Nat. Energy 6 (4), 388–397.

Zhou, P., Navid, I.A., Ma, Y., Xiao, Y., Wang, P., Ye, Z., Zhou, B., Sun, K., Mi, Z., 2023. Solar-to-hydrogen efficiency of more than 9% in photocatalytic water splitting. Nature 613 (7942), 66–70.